Enhancement of microwave to optical spin-based quantum transduction via a magnon mode

Tharnier O. Puel,[1] Adam T. Turflinger,[2] Sebastian P. Horvath,[2] Jeff D. Thompson,[2] and Michael E. Flatté[1,3]
[1]Department of Physics and Astronomy, University of Iowa, Iowa 52242, USA
[2]Department of Electrical and Computer Engineering, Princeton University, New Jersey 08544, USA
[3]Department of Applied Physics, Eindhoven University of Technology, Eindhoven, The Netherlands

(Received 19 November 2024; revised 8 April 2025; accepted 30 May 2025; published 4 September 2025)

We propose a method for converting single microwave photons to single optical sideband photons based on spinful impurities in magnetic materials. This hybrid system is advantageous over previous proposals because (i) the implementation allows much higher transduction rates (10^3 times faster at the same optical pump Rabi frequency) than state-of-the-art devices, (ii) high-efficiency transduction is found to happen in a significantly larger space of device parameters (in particular, over 1 GHz microwave detuning), and (iii) it does not require mode volume matching between optical and microwave resonators. We identify the needed magnetic interactions as well as potential materials systems to enable this speed up using erbium dopants for telecom compatibility. This is an important step towards realizing high-fidelity entangling operations between remote qubits and will provide additional control of the transduction through perturbation of the magnet.

DOI: 10.1103/kqw2-gs9c

I. INTRODUCTION

Coherent transduction of microwave photons to optical photons [1], hereafter for concision "quantum transduction," will enable scaling of dilution-fridge (e.g., superconducting [2]) quantum processors via remote entangling operations over room-temperature optical fiber. Demonstrated quantum transduction platforms include optomechanical transducers, [3–5], the electro-optic effect in lithium niobate [6], the magneto-optic effect in $Y_3Fe_5O_{12}$ (YIG) [7,8], Rydberg atom clouds [9–11], and dilute ensembles of rare-earth ions in a crystal [12–16]. Optomechanical transduction enabled the first optical readout of Rabi oscillations in a superconducting qubit [17,18], lithium niobate transducers have achieved moderate conversion efficiencies with the introduction of only a small amount of conversion noise and MHz bandwidth [19,20], Rydberg atom transducers have demonstrated near-unit-efficiency frequency conversion between microwave and optical photons with high bandwidth, and rare-earth ions (particularly using Er for telecom wavelength compatibility) have demonstrated coherent chip-integrated wavelength transducers. However, each of these approaches faces critical challenges in achieving high efficiency, bandwidth well matched to the 10–100 ns timescale for gate operations in superconducting qubits [21], and integration with superconducting qubits in the same device. The optical pump necessary to bridge the frequency gap between microwave and optical photons specifically creates notable technical issues including heating [22] and destruction of Cooper pairs in superconducting circuits [23] leading to noise and reduced efficiencies. Rare-earth ion transducers have produced high efficiencies at MHz-scale bandwidths [16], but scaling to repetition rates beyond the kHz level with quantum-limited photon noise will require higher coupling between the ensemble and microwave photons as well as the mitigation of heating from the optical pump.

Direct transduction using magnets has been proposed before [24–26] on account of their strong coupling to microwave photons (e.g., in YIG [27,28] and $GdVO_4$ [28]). However, these crystals lack the sharp optical lines of rare-earth ions, so the transducers are limited by the weak Brillouin scattering interaction between optical photons and magnons in spite of the high microwave photon couplings [24–26,28–31]. Alternatively, fully concentrated rare-earth crystals leverage the strong coupling of microwave photons to magnons and the optical transitions of rare-earth ions [32], but demonstrating frequency conversion has been a challenge on account of the very high optical density of the fully concentrated rare-earth crystals [33]. Finally, recent developments have been made towards antiferromagnetic optomagnonics [34,35].

We propose to overcome the weak optical interaction of magnets using dilute doping of an optically active defect into a magnetic material, maintaining the strong microwave-magnon coupling while enhancing the optical coupling via the defects. This proposal relies on attainable narrow microwave linewidths in magnets [36–39] and optical linewidths in rare-earth ensembles [40–45], and we effectively reduce the problem to creating an appropriate interaction between the magnet and dopants within several proposed materials. We demonstrate how the strengthened coupling, to both single microwave and optical photons, enables transducers with significantly increased effective transduction rates (as much as 10^3 times faster at the same optical pump Rabi frequency) and bandwidths (∼1 GHz microwave detunings) compared

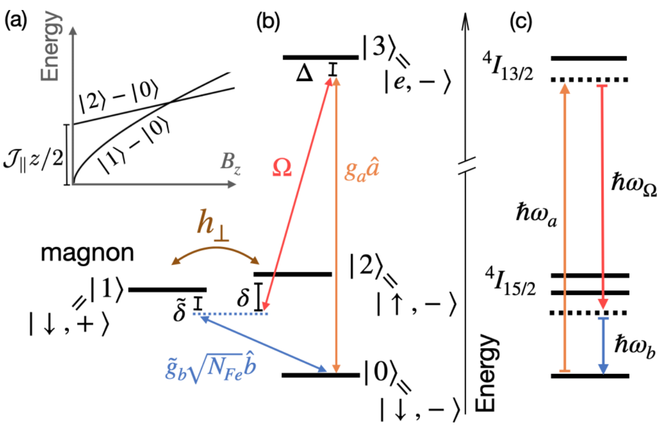

FIG. 1. (a) Crossing between the magnon excitation ($|0\rangle \to |1\rangle$) and the erbium-spin flip ($|0\rangle \to |2\rangle$) versus B_z. (b) Full energy-level diagram, including the erbium excited state ($|3\rangle$), and the transitions due to the couplings to an optical cavity ($g_a\hat{a}$), to an optical pump (Ω), to a magnon via spin exchange ($h_\perp$), and to a magnon via the microwave cavity ($\tilde{g}_b\sqrt{N_{\rm Fe}}\hat{b}$). $\tilde{\delta}$, δ, and Δ are detuning parameters to the cavity frequencies. (c) Frequencies of the optical cavity resonance (ω_a), microwave resonator (ω_b), and optical pump (ω_Ω).

to prior art. These improvements will enable higher-fidelity remote entangling operations of superconducting qubits that approach the threshold for entanglement purification [46].

The enhancement of the transduction can be derived from the linear combination of optically active single-spin defects interacting with the spins in a magnet. Without loss of generality we first assume a single erbium ion within a YIG magnet (represented by the Fe atoms) in the presence of a static magnetic field, as well as microwave (MW) and optical (opt) fields, as schematically presented in Fig 1.

II. HAMILTONIAN

The system above can be described with the Hamiltonian

$$\mathcal{H}(t) = \mathcal{H}_0 + \mathcal{H}_{\rm Zee} + \mathcal{H}_{\rm ex} + \mathcal{H}_{\rm opt}(t) + \mathcal{H}_{\rm MW}(t), \quad (1)$$

where $\mathcal{H}_0 = \mathcal{H}_{\rm Fe} + \mathcal{H}_{\rm Er}$ is the total energy of all iron atoms and a single erbium ion in a crystal. $\mathcal{H}_{\rm Zee}$ is the Zeeman term due to the presence of an external static field B_z along the z direction. The exchange interaction $\mathcal{H}_{\rm ex}$ between the single erbium spin and its z nearest neighbors (n.n.) iron atoms is assumed to have the following anisotropic form

$$\mathcal{H}_{\rm ex} = -\frac{1}{\hbar^2}\boldsymbol{S}^{\rm Er}\cdot\boldsymbol{\mathcal{J}}\cdot\sum_{i\in{\rm n.n.}}\boldsymbol{S}_i^{\rm Fe},$$
$$\approx -\frac{z\mathcal{J}_\perp}{2\hbar^2}\left(S_+^{\rm Er}S_{i,-}^{\rm Fe} + S_-^{\rm Er}S_{i,+}^{\rm Fe}\right) - \frac{z\mathcal{J}_\parallel}{\hbar^2}S_z^{\rm Er}S_{i,z}^{\rm Fe}, \quad (2)$$

$\forall\, i \in$ n.n. The $\boldsymbol{S}_i^{\rm Fe}$ is the magnetic moment of the i-th iron atom and $\boldsymbol{S}^{\rm Er}$ the pseudospin operator of a single erbium ion. The term with exchange coupling $\mathcal{J}_\parallel$ contributes to the Zeeman energy and $\mathcal{J}_\perp$ to the exchange of excitation between spins, i.e., converting a magnetic excitation into an erbium spin-flip transition. The $\mathcal{H}_{\rm opt}(t)$ accounts for the interaction between the optical fields and the Er ion. The two oscillating optical fields, $\boldsymbol{E}_a(t)$ and $\boldsymbol{E}_\Omega(t)$, couple the ground and first excited manifolds ($^4{\rm I}_{15/2}-{}^4{\rm I}_{13/2}$) of the erbium ion through an effective electric dipole operator ($\boldsymbol{\mu}^{\rm Er}$) as

$$\mathcal{H}_{\rm opt}(t) = -\boldsymbol{\mu}^{\rm Er}\cdot\boldsymbol{E}_a(t) - \boldsymbol{\mu}^{\rm Er}\cdot\boldsymbol{E}_\Omega(t). \quad (3)$$

Here, $\boldsymbol{E}_\Omega(t) = E_\Omega\cos(\omega_\Omega t)\hat{\boldsymbol{e}}_\Omega$ is an external pump field and $\boldsymbol{E}_a(t) = E_a\cos(\omega_a t)\hat{\boldsymbol{e}}_a$ is an upconverted optical sideband field. In addition, the $\mathcal{H}_{\rm MW}(t)$ accounts for the presence of a microwave field, $\boldsymbol{B}_b(t) = B_b\cos(\omega_b t)\hat{\boldsymbol{e}}_b$, that couples to both erbium and iron spins via their magnetic dipole moments as

$$\mathcal{H}_{\rm MW}(t) = \left(\mu_B g_S\hbar^{-1}\sum_{i=1}^{N_{\rm Fe}}\boldsymbol{S}_i^{\rm Fe} + \mu_B g_J\hbar^{-1}\boldsymbol{S}^{\rm Er}\right)\cdot\boldsymbol{B}_b(t), \quad (4)$$

where $N_{\rm Fe}$ is the total number of spins in the magnet volume, and g_S and g_J are the g factors of the iron spins and the erbium spins in the manifold with total angular momentum J, respectively.

The Hamiltonian in Eq. (1) acts on the reduced erbium ion energy levels $|\downarrow\rangle \equiv |J = 15/2, m_S = -1/2\rangle$, $|\uparrow\rangle \equiv |J = 15/2, m_S = +1/2\rangle$, and $|e\rangle \equiv |J = 13/2, m_S = -1/2\rangle$, where m_S is the pseudospin related to the lowest-energy doublet within the multiplet J. It also acts on the ground and first excited states of the magnet, which are $|-\rangle \equiv |\downarrow\ldots\downarrow\rangle$ and $|+\rangle \equiv N_{\rm Fe}^{-1/2}\sum_{i=1}^{N_{\rm Fe}}|\downarrow\ldots\uparrow_i\ldots\downarrow\rangle$. These two states describe the uniform mode of the magnet, a magnon, in which the spins presses coherently around the z axis, corresponding to an isotropic configuration with respect to $\hat{z}$. Alternative configurations, including anisotropy, have been discussed in Refs. [47,48]. The ground-state energy of the composite system is $E_\downarrow \equiv \langle\downarrow,-|\mathcal{H}|\downarrow,-\rangle$. An energy level diagram is illustrated in Fig. 1(a). We are particularly interested in the magnetic excitation energy $E_m \equiv \langle\downarrow,+|\mathcal{H}|\downarrow,+\rangle$ and the first spin excitation $E_\uparrow \equiv \langle\uparrow,-|\mathcal{H}|\uparrow,-\rangle$ relative to the ground state, i.e.,

$$E_m - E_\downarrow = \gamma\sqrt{B_z(B_z + M_s)} - \frac{z\mathcal{J}_\parallel}{2N_{\rm Fe}}, \quad (5)$$

$$E_\uparrow - E_\downarrow = \mu_B g_g B_z + \frac{z\mathcal{J}_\parallel}{2}, \quad (6)$$

where the square root in Eq. (5) follows the Kittel formula [49,50] for the magnetic excitation of a thin film, in which γ is the gyromagnetic ratio and M_S is the saturation magnetization. Here $g_g \equiv g_{J=15/2}$. Notably, the Ising exchange coupling $\mathcal{J}_\parallel$ acts as an effective static magnetic field significantly changing the energy of the erbium-spin transition [Eq. (6)], but has little effect on the magnon resonance frequency as it is normalized by the total number of spins in the magnet, notice $\mathcal{J}_\parallel/N_{\rm Fe}$ in Eq. (5). Finally, the magnon and erbium spins must be near resonance in order to allow magnon-erbium flip flops within the secular approximation. Thus, the exchange interaction $\mathcal{J}_\parallel$ must be small enough to allow for the intersection of the Er and magnon resonances at an experimentally feasible magnetic field. Additionally, even in the absence of $\mathcal{J}_\parallel$, in the large B_z limit the spin ensemble g factor is constrained to $\mu_B g_g < \gamma$ for an anticrossing to occur. The following results assume a microwave frequency, set by $\boldsymbol{B}_b(t)$, to be mutually detuned from magnon and spin resonant frequencies in Eqs. (5) and (6).

III. HAMILTONIAN IN CAVITY QED NOTATION

First, we relabel the erbium states $|0\rangle \equiv |\downarrow, -\rangle$, $|2\rangle \equiv |\uparrow, -\rangle$, and $|3\rangle \equiv |e, -\rangle$, and the magnon state $|1\rangle \equiv |\downarrow, +\rangle$, see Fig. 1. Second, we write the Hamiltonian in terms of transition operators $\hat{\sigma}_{i,j} \equiv |i\rangle\langle j|$, with $i, j = 0, 1, 2, 3$. Third, we define the transition elements

$$\langle 1|\mathcal{H}(t)|2\rangle = \hbar h_\perp N_{\rm Fe}^{-1/2}\langle 1|\hat{\sigma}_{1,2}|2\rangle, \tag{7}$$

$$\langle 0|\mathcal{H}(t)|2\rangle = \hbar \mathrm{g}_b 2\cos(\omega_b t)\langle 0|\hat{\sigma}_{0,2}|2\rangle, \tag{8}$$

$$\langle 0|\mathcal{H}(t)|1\rangle = \hbar \tilde{\mathrm{g}}_b N_{\rm Fe}^{1/2} 2\cos(\omega_b t)\langle 0|\hat{\sigma}_{0,1}|1\rangle, \tag{9}$$

$$\langle 0|\mathcal{H}(t)|3\rangle = \hbar \mathrm{g}_a 2\cos(\omega_a t)\langle 0|\hat{\sigma}_{0,3}|3\rangle, \tag{10}$$

$$\langle 2|\mathcal{H}(t)|3\rangle = \hbar \Omega 2\cos(\omega_\Omega t)\langle 2|\hat{\sigma}_{2,3}|3\rangle, \tag{11}$$

related to the previous quantities as $\hbar \mathrm{g}_b = \mu_B g_g \beta_- B_b/4$, $\hbar\tilde{\mathrm{g}}_b = \mu_B g_S B_b/4$, $\hbar \mathrm{g}_a = \mu^{\rm Er} E_a/2$, $\hbar\Omega = \mu^{\rm Er} E_\Omega/2$, and $\hbar h_\perp = -\mathcal{J}_\perp z\beta_-/2$ (details in the Supplemental Material (SM) [51]). The new variables g_b, $\tilde{\mathrm{g}}_b$, g_a, and $h_\perp$ have values of coupling per spin, and Ω is the optical pump Rabi frequency (or the pump power $\propto \Omega^2$). From that, we build a new Hamiltonian $\mathcal{H}'(t) = \sum_{i,j}\langle i|\mathcal{H}(t)|j\rangle|i\rangle\langle j|$. The time dependence can be removed using the rotating-wave approximation (RWA) [52] ($e^{-i2\omega t} \approx 0$, see SM [51]), taking $\mathcal{H}'(t) \to \mathcal{H}_{\rm RWA}$. The energy levels are then defined with respect to their detunings from the wave frequencies, namely, we define $\hbar\delta = (E_\uparrow - E_\downarrow) - \hbar\omega_b$, $\hbar\tilde{\delta} = (E_m - E_\downarrow) - \hbar\omega_b$, and $\hbar\Delta = (E_e - E_\downarrow) - \hbar\omega_a$, with $\omega_a = \omega_\Omega + \omega_b$, as illustrated in Fig. 1. The Hamiltonian can then be written as

$$\mathcal{H}_{\rm RWA} = \hbar \begin{pmatrix} 0 & \tilde{\mathrm{g}}_b N_{\rm Fe}^{1/2} & \mathrm{g}_b & \mathrm{g}_a \\ \tilde{\mathrm{g}}_b^* N_{\rm Fe}^{1/2} & \tilde{\delta} & h_\perp N_{\rm Fe}^{-1/2} & 0 \\ \mathrm{g}_b^* & h_\perp^* N_{\rm Fe}^{-1/2} & \delta & \Omega \\ \mathrm{g}_a^* & 0 & \Omega^* & \Delta \end{pmatrix}. \tag{12}$$

Next, we suppose that the crystal is embedded in both an optical cavity (of frequency ω_a) and a microwave resonator (of frequency ω_b), such that there will be an exchange of photons between the microwave transitions and the resonator (i.e., $\hat{\sigma}_{0,1} \to \hat{\sigma}_{0,1}\hat{b}^\dagger$ and $\hat{\sigma}_{0,2} \to \hat{\sigma}_{0,2}\hat{b}^\dagger$), as well as the optical transition and the cavity (i.e., $\hat{\sigma}_{0,3} \to \hat{\sigma}_{0,3}\hat{a}^\dagger$). The optical pump field is tuned to create a three photon resonance between the microwave and optical cavity fields, i.e., $\omega_b + \omega_\Omega = \omega_a$. These transitions are schematically represented in Fig. 1(c).

The Hilbert space including the cavity and the resonator becomes $|\psi\rangle = |\mathrm{Er}, \mathrm{Fe}\rangle|b\rangle|a\rangle$, from which we build a new Hamiltonian $\mathcal{H}'_{\rm RWA} = \sum_{i,j}\langle i|\mathcal{H}_{\rm RWA}|j\rangle|i\rangle\langle j|$. Solving the Eqs. of motion $i\hbar\partial_t|\psi(t)\rangle = \mathcal{H}'_{\rm RWA}|\psi(t)\rangle$, using adiabatic elimination of the higher-energy states [53–55] ($|\tilde{\delta}| \gg |\tilde{\mathrm{g}}|, |h|$, and $|\delta| \gg |\Omega|, |\mathrm{g}_b|, |h|$, and $|\Delta| \gg |\mathrm{g}_a|, |\Omega|$, with $\tilde{\mathrm{g}} = \tilde{\mathrm{g}}_b N_{\rm Fe}^{1/2}$ and $h = h_\perp N_{\rm Fe}^{-1/2}$, see SM [51]), we end up with an effective Hamiltonian of the form $\mathcal{H}_{\rm eff} = i(\kappa_a/2)\hat{a}^\dagger\hat{a} + i(\kappa_b/2)\hat{b}^\dagger\hat{b} + S^*\hat{a}^\dagger\hat{b} + S\hat{b}^\dagger\hat{a}$, where κ_a, κ_b are photon leakage rates of the optical cavity and the microwave resonator, respectively, and S is the transduction rate. As the pump power is a limiting constraint in practical transduction implementations, here we focus on the normalized transduction rate S/Ω, corresponding to the transduction rate normalized by the pump Rabi frequency. The linear combination of erbium-ion-spin ensemble, $N_{\rm Er}$, results in

$$\frac{S}{\Omega} = \frac{N_{\rm Er}(\tilde{\delta}\mathrm{g}_b - h_\perp\tilde{\mathrm{g}}_b)\mathrm{g}_a}{\Delta(\delta\tilde{\delta} - h_\perp^2 N_{\rm Fe}^{-1})}. \tag{13}$$

Notice that the limit $h_\perp \to 0$ recovers the result in Ref. [56]. Via the input-output formalism we introduce the operators $\hat{a}_{\rm in}, \hat{a}_{\rm out}, \hat{b}_{\rm in}, \hat{b}_{\rm out}$, from which we extract the efficiency ($\eta = 2\sqrt{\mathcal{C}}/(1+\mathcal{C})$) and cooperativity [$\mathcal{C} = 4|S|^2/(\kappa_a\kappa_b)$], see SM [51]. In this scenario, the unit efficiency happens when the transduction rate is matched to the cavities leakage, i.e., the so-called impedance matching condition $2|S| = \sqrt{\kappa_a\kappa_b}$, thus $\mathcal{C} = 1$ and $\eta = 1$. As we are going to show next, higher rates κ_a and κ_b are desirable to achieve higher transduction rates, mitigating the losses and leading to larger bandwidths. Our main findings in this paper come from exploring the limit $|h_\perp\tilde{\mathrm{g}}_b| \gg |\tilde{\delta}\mathrm{g}_b|$ for obtaining higher transduction rates. If we further separate the leakage into an extrinsic leakage (henceforth called coupling rate) $\kappa_{a,c}, \kappa_{b,c}$ and an intrinsic device loss $\kappa_{a,i}, \kappa_{b,i}$, the efficiency is computed as (more details in the SM [51])

$$\eta = \frac{4|S|\sqrt{\kappa_{a,c}\kappa_{b,c}}}{(\kappa_{a,c}+\kappa_{a,i})(\kappa_{b,c}+\kappa_{b,i}) + 4|S|^2}. \tag{14}$$

Notice that 100% efficiency is achieved at the impedance match condition only for zero intrinsic losses, i.e., $\kappa_{a,i} = \kappa_{b,i} = 0$, however, the intrinsic losses in a device can be mitigated by a high ratio of cavity coupling to intrinsic loss $\kappa_{(a,b),c}/\kappa_{(a,b),i} \gg 1$.

IV. CALCULATIONS

In the following we show some quantitative results to illustrate magnon enhancement of rare-earth quantum transduction processes. We compare the normalized transduction rate (S/Ω) with and without the presence of a magnet, for the idealized case of erbium-iron perpendicular interaction $\mathcal{J}_\perp = 1$ THz and Ising interaction $\mathcal{J}_\parallel = 1$ GHz. Then, we vary the erbium-iron perpendicular interaction, showing how the results connect to the case of smaller exchange anisotropy (for $\mathcal{J}_\perp \approx \mathcal{J}_\parallel \approx$ GHz). Finally, we show how our proposal allows higher coupling rates at much lower pump power than previous proposals.

A strong exchange interaction between erbium and iron of $\mathcal{J} \approx 0.714$ THz has been observed in erbium orthoferrite ($ErFeO_3$) [57]. Similarly, the spin-flop transition in Er:YIG observed at 30 K is indicative of a strong Er-Fe coupling of $\mathcal{J} \approx 0.625$ THz [58]. However, so far there is no evidence of anisotropy, i.e., $\mathcal{J}_\perp = \mathcal{J}_\parallel = \mathcal{J}$ in these materials. Such a strong parallel coupling shifts the spin transition away from the typical $\sim$10 GHz for superconducting qubits, as discussed in Fig. 1(a). Therefore, our proposal suggests that finding a system with Er-Fe coupling of $\mathcal{J}_\parallel \approx 1$ GHz would be ideal, while keeping $\mathcal{J}_\perp \approx 1$ THz. The strong perpendicular exchange coupling is favorable because it leads to the limit $|h_\perp\tilde{\mathrm{g}}_b| \gg |\tilde{\delta}\mathrm{g}_b|$ in Eq. (13), whereas the opposite limit recovers the nonmagnetic transducer in Ref. [56].

Figure 2 shows S/Ω varying with the external parameters, the resonator frequency (ω_b) and the static magnetic field B_z, for the cases Fig. 2(a) without a magnet and Fig. 2(b)

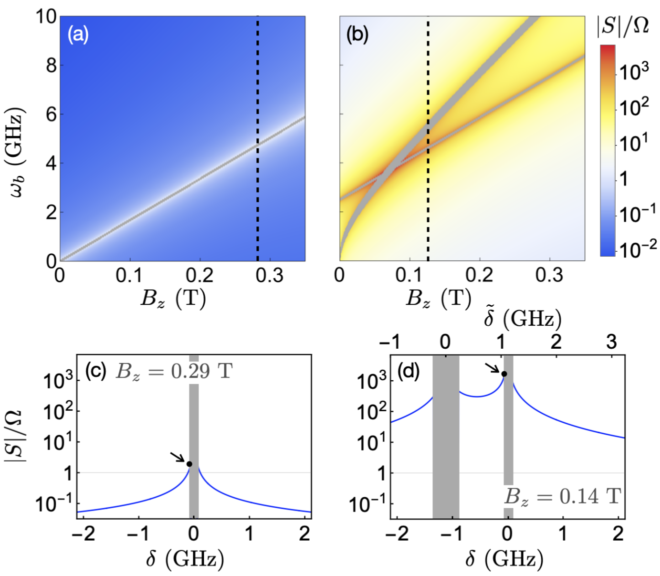

FIG. 2. Normalized transduction rate ($|S|/\Omega$) versus B_z and the microwave frequency ω_b, (a) without and (b) with a magnet. The gray stripes cover the regions where the adiabatic elimination approximation fails. Vertical-dashed lines indicate the B_z values used in (c) and (d), which show $|S|/\Omega$ versus the detunings δ and $\tilde{\delta}$ for $\omega_b \approx 5$ GHz near the erbium-spin-magnon resonance. The black points (see arrows) highlight the maximum transduction rates used in Fig. 3.

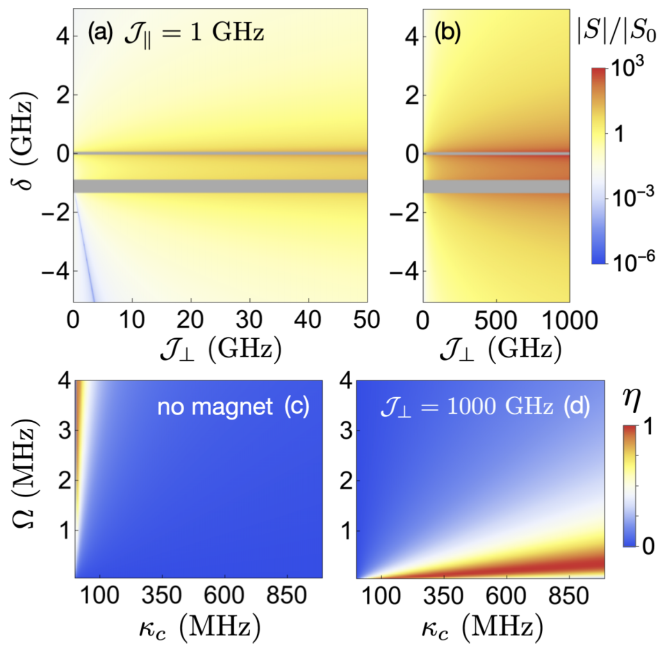

FIG. 3. (a) Transduction rate in the presence of a magnet ($|S|$) relative to the maximum value without a magnet $|S_0|$, represented by a point in Fig. 2(c), versus detuning (δ) and spin-exchange interaction ($\mathcal{J}_\perp$). (b) Same as (a) over larger range of $\mathcal{J}_\perp$. Gray stripes same as in Fig. 2. Blue feature in (a) for $\delta < 0$ and small $\mathcal{J}_\perp$ is due to $|S| \to 0$ for $\tilde{\delta} g_b \approx h_\perp \tilde{g}_b$, see Eq. (13). (c) and (d) Efficiency (η) versus Ω and coupling rates ($\kappa_{a,c} = \kappa_{b,c} \equiv \kappa_c$) at the $|S_0|$ values marked in Figs. 2(c) and 2(d), respectively.

with a magnet. For a certain set of parameters, the system reaches a resonant condition ($\delta = 0$ or $\tilde{\delta} = 0$) between the microwave resonator and either the spin or the magnon excitations. As the detunings reach zero, the adiabatic elimination condition is broken, populating the excited state and causing the microwave photon to be parasitically absorbed. Thus, gray areas are added to block regions within five linewidths of spin and magnon transitions, see SM [51] for a list of parameters used. Comparing Figs. 2(a) and 2(b), we see that S/Ω reaches orders of magnitude higher values in the presence of a magnet. From Figs. 2(c) and 2(d) we notice that higher rates are especially large near the crossing between the magnon and the spin transition frequencies, thus close to the adiabatic elimination condition limits. Also, the presence of a magnet allows $|S/\Omega| > 10^2$ for over 1 GHz microwave detuning range.

Next, we explore the case of $\mathcal{J}_\parallel \approx \mathcal{J}_\perp \approx$ GHz, that represents a magnet with weaker spin-exchange couplings, or spin-magnet dipole coupling as will be discussed below. In Figs. 3(a) and 3(b) we show the transduction rate in the presence of a magnet, relative to the maximum transduction rate obtained without a magnet [defined as $|S_0|$ and marked as a black point in Fig. 2(c)], as we vary the perpendicular exchange coupling. It becomes clear that the presence of a magnet leads to higher transduction rates overall, even for lower values of $\mathcal{J}_\perp$, in which we see an increase of two orders of magnitude at detunings close to the adiabatic elimination condition. The feature appearing in Fig. 3(a) for negative detuning ($\delta < -1$ GHz) and small coupling values ($\mathcal{J}_\perp < 5$ GHz) is due to the reduced transduction rate approaching zero for $\tilde{\delta} g_b \approx h_\perp \tilde{g}_b$, see Eq. (13).

To better quantify the advantages of using a magnet in the transduction process, in Figs. 3(c) and 3(d), we analyze the transduction efficiency, see Eq. (14), as we vary the optical pump (Ω) and the coupling rates ($\kappa_{a,c} = \kappa_{b,c} \equiv \kappa_c$). The red region signals the near unit efficiency, where the impedance matching condition is satisfied, $2|S| = \kappa_c$. The linear behavior in this region is the result of $\mathcal{J}_\perp = 1$ THz, thus $|h_\perp \tilde{g}_b| \gg |\tilde{\delta} g_b|$, and the impedance matching condition leads to

$$\frac{\kappa_c}{\Omega} = \left| \frac{N_{\mathrm{Er}} h_\perp \tilde{g}_b g_a}{\Delta \delta \tilde{\delta}} \right|, \qquad \text{(with magnet)} \qquad (15)$$

$$\frac{\kappa_c}{\Omega} = \left| \frac{N_{\mathrm{Er}} g_b g_a}{\Delta \delta} \right|, \qquad \text{(without magnet).} \qquad (16)$$

Thus, the magnet allows the maximum efficiency to be achieved at significantly lower pump powers and significantly higher cavity coupling rates.

In addition to the advantages discussed above, our proposed scheme also removes any rate penalty from mismatched optical and microwave mode volumes [59]. This is because the microwave resonator needs to be coupled only to the iron atoms in the magnet and not the erbium ions. This removes a significant experimental challenge in designing colocalized optical and microwave photons, and also opens new possibilities for transduction device implementations, particularly with small mode volume and spatially separated optical cavities. Freedom in choice of optical cavities is particularly important as pump-induced heating [22] and optical destruction of

Cooper pairs in superconducting microwave resonators [23] have proven to be significant challenges in experimental microwave to optical transducers.

V. DISCUSSION

In the following we discuss possible routes to achieve a rare-earth magnet interaction required to realize our proposal. It is first necessary to create an erbium spin-magnon resonance at an experimentally reasonable field. This is most easily achieved if $\mathcal{J}_\parallel \approx$ GHz. One such approach would use a dipole-dipole interaction instead of exchange. For example, consider a heterostructure composed of a thin film of YIG on a substrate of Er:YAG, thus positioning the Er near to the magnet's surface and leading to strong erbium-spin-iron-spin interaction (we estimate ∼10 nm for a ∼GHz coupling strength) [60–62].

A far larger transduction improvement would be achieved with large exchange anisotropy ($\mathcal{J}_\perp \gg \mathcal{J}_\parallel$). For example, the Dzyaloshinskii-Moriya interaction (DMI) induces spin transitions as $(S_1^+S_2^- - S_1^-S_2^+)$, see SM [51]. Thus, for magnets with $\mathcal{J}_\parallel \approx$ GHz, the DMI enhances the spin transitions to fulfill our requirement $\mathcal{J}_\perp \gg \mathcal{J}_\parallel$. However, the Fe-$Er^{3+}$ DMI has not been measured. Although the rare-earth g tensors are known to have anisotropies that exceed ten in noncubic site [63,64], the anisotropy of the exchange interaction itself is not well studied; to our knowledge, more material characterization is necessary for finding anisotropic couplings with lower strengths ($\mathcal{J}_\parallel \approx$ GHz).

Alternatively, there has been interest in using millimeter-wave qubits instead of microwave-frequency qubits for easier transduction [11,65]. Our analysis directly extends to millimeter-wave magnons in which strong $\mathcal{J}_\parallel \sim 100$ GHz is needed to obtain resonance between the erbium spin ensemble and the magnon.

We have proposed that the strong coupling between spinful optically active impurities and a magnon can implement high-efficiency transduction at rates at least two orders of magnitude faster than existing approaches based on dilute rare-earth ion ensembles.

ACKNOWLEDGMENTS

This work is supported by the U.S. Department of Energy, Office of Science: theoretical analysis of magnon mode enhancement of microwave-to-optical transduction by BES Award No. DE-SC0023393, magnon-erbium spin coupling by BES Award No. DE-SC0019250, and identifying advantages relative to alternative approaches by the NQISRC Co-design Center for Quantum Advantage (C2QA) under Contract No. DE-SC0012704.

[1] Z.-L. Xiang, S. Ashhab, J. Q. You, and F. Nori, Hybrid quantum circuits: Superconducting circuits interacting with other quantum systems, Rev. Mod. Phys. **85**, 623 (2013).

[2] F. Arute, K. Arya, R. Babbush, D. Bacon, J. C. Bardin, R. Barends, R. Biswas, S. Boixo, F. G. S. L. Brandao, D. A. Buell, B. Burkett, Y. Chen, Z. Chen, B. Chiaro, R. Collins, W. Courtney, A. Dunsworth, E. Farhi, B. Foxen, A. Fowler *et al.*, Quantum supremacy using a programmable superconducting processor, Nature (London) **574**, 505 (2019).

[3] T. Bagci, A. Simonsen, S. Schmid, L. G. Villanueva, E. Zeuthen, J. Appel, J. M. Taylor, A. Sørensen, K. Usami, A. Schliesser, and E. S. Polzik, Optical detection of radio waves through a nanomechanical transducer, Nature (London) **507**, 81 (2014).

[4] R. W. Andrews, R. W. Peterson, T. P. Purdy, K. Cicak, R. W. Simmonds, C. A. Regal, and K. W. Lehnert, Bidirectional and efficient conversion between microwave and optical light, Nat. Phys. **10**, 321 (2014).

[5] J. Bochmann, A. Vainsencher, D. D. Awschalom, and A. N. Cleland, Nanomechanical coupling between microwave and optical photons, Nat. Phys. **9**, 712 (2013).

[6] A. Rueda, F. Sedlmeir, M. C. Collodo, U. Vogl, B. Stiller, G. Schunk, D. V. Strekalov, C. Marquardt, J. M. Fink, O. Painter, G. Leuchs, and H. G. L. Schwefel, Efficient microwave to optical photon conversion: An electro-optical realization, Optica **3**, 597 (2016).

[7] R. Hisatomi, A. Osada, Y. Tabuchi, T. Ishikawa, A. Noguchi, R. Yamazaki, K. Usami, and Y. Nakamura, Bidirectional conversion between microwave and light via ferromagnetic magnons, Phys. Rev. B **93**, 174427 (2016).

[8] X. Zhang, N. Zhu, C.-L. Zou, and H. X. Tang, Optomagnonic whispering gallery microresonators, Phys. Rev. Lett. **117**, 123605 (2016).

[9] J. Han, T. Vogt, C. Gross, D. Jaksch, M. Kiffner, and W. Li, Coherent microwave-to-optical conversion via six-wave mixing in Rydberg atoms, Phys. Rev. Lett. **120**, 093201 (2018).

[10] H.-T. Tu, K.-Y. Liao, Z.-X. Zhang, X.-H. Liu, S.-Y. Zheng, S.-Z. Yang, X.-D. Zhang, H. Yan, and S.-L. Zhu, High-efficiency coherent microwave-to-optics conversion via off-resonant scattering, Nat. Photon. **16**, 291 (2022).

[11] A. Kumar, A. Suleymanzade, M. Stone, L. Taneja, A. Anferov, D. I. Schuster, and J. Simon, Quantum-enabled millimetre wave to optical transduction using neutral atoms, Nature (London) **615**, 614 (2023).

[12] X. Fernandez-Gonzalvo, Y.-H. Chen, C. Yin, S. Rogge, and J. J. Longdell, Coherent frequency up-conversion of microwaves to the optical telecommunications band in an Er:YSO crystal, Phys. Rev. A **92**, 062313 (2015).

[13] X. Fernandez-Gonzalvo, S. P. Horvath, Y.-H. Chen, and J. J. Longdell, Cavity-enhanced Raman heterodyne spectroscopy in Er^{3+}:Y_2SiO_5 for microwave to optical signal conversion, Phys. Rev. A **100**, 033807 (2019).

[14] J. G. Bartholomew, J. Rochman, T. Xie, J. M. Kindem, A. Ruskuc, I. Craiciu, M. Lei, and A. Faraon, On-chip coherent microwave-to-optical transduction mediated by ytterbium in YVO_4, Nat. Commun. **11**, 3266 (2020).

[15] J. Rochman, T. Xie, J. G. Bartholomew, K. C. Schwab, and A. Faraon, Microwave-to-optical transduction with erbium ions coupled to planar photonic and superconducting resonators, Nat. Commun. **14**, 1153 (2023).

[16] T. Xie, R. Fukumori, J. Li, and A. Faraon, Scalable microwave-to-optical transducers at the single-photon level with spins, Nat. Phys. **21**, 931 (2025).

[17] M. Mirhosseini, A. Sipahigil, M. Kalaee, and O. Painter, Superconducting qubit to optical photon transduction, Nature (London) **588**, 599 (2020).

[18] R. D. Delaney, M. D. Urmey, S. Mittal, B. M. Brubaker, J. M. Kindem, P. S. Burns, C. A. Regal, and K. W. Lehnert, Superconducting-qubit readout via low-backaction electro-optic transduction, Nature (London) **606**, 489 (2022).

[19] L. Fan, C.-L. Zou, R. Cheng, X. Guo, X. Han, Z. Gong, S. Wang, and H. X. Tang, Superconducting cavity electro-optics: A platform for coherent photon conversion between superconducting and photonic circuits, Sci. Adv. **4**, eaar4994 (2018).

[20] R. Sahu, W. Hease, A. Rueda, G. Arnold, L. Qiu, and J. M. Fink, Quantum-enabled operation of a microwave-optical interface, Nat. Commun. **13**, 1276 (2022).

[21] A. P. M. Place, L. V. H. Rodgers, P. Mundada, B. M. Smitham, M. Fitzpatrick, Z. Leng, A. Premkumar, J. Bryon, A. Vrajitoarea, S. Sussman, G. Cheng, T. Madhavan, H. K. Babla, X. H. Le, Y. Gang, B. Jäck, A. Gyenis, N. Yao, R. J. Cava, N. P. de Leon *et al.*, New material platform for superconducting transmon qubits with coherence times exceeding 0.3 milliseconds, Nat. Commun. **12**, 1779 (2021).

[22] K. Azuma, K. Tamaki, and H.-K. Lo, All-photonic quantum repeaters, Nat. Commun. **6**, 6787 (2015).

[23] M. Xu, C. Li, Y. Xu, and H. X. Tang, Light-induced microwave noise in superconducting microwave-optical transducers, Phys. Rev. Appl. **21**, 014022 (2024).

[24] S. V. Kusminskiy, H. X. Tang, and F. Marquardt, Coupled spin-light dynamics in cavity optomagnonics, Phys. Rev. A **94**, 033821 (2016).

[25] F. Engelhardt, V. A. S. V. Bittencourt, H. Huebl, O. Klein, and S. V. Kusminskiy, Optimal broadband frequency conversion via a magnetomechanical transducer, Phys. Rev. Appl. **18**, 044059 (2022).

[26] T. Liu, X. Zhang, H. X. Tang, and M. E. Flatté, Optomagnonics in magnetic solids, Phys. Rev. B **94**, 060405 (2016).

[27] A. Ghirri, C. Bonizzoni, M. Maksutoglu, A. Mercurio, O. Di Stefano, S. Savasta, and M. Affronte, Ultrastrong magnon-photon coupling achieved by magnetic films in contact with superconducting resonators, Phys. Rev. Appl. **20**, 024039 (2023).

[28] J. R. Everts, G. G. G. King, N. J. Lambert, S. Kocsis, S. Rogge, and J. J. Longdell, Ultrastrong coupling between a microwave resonator and antiferromagnetic resonances of rare-earth ion spins, Phys. Rev. B **101**, 214414 (2020).

[29] X. Zhang, N. Zhu, C.-L. Zou, and H. X. Tang, Erratum: Optomagnonic whispering gallery microresonators [Phys. Rev. Lett. 117, 123605 (2016)], Phys. Rev. Lett. **121**, 199901(E) (2018).

[30] N. Zhu, X. Zhang, X. Han, C.-L. Zou, C. Zhong, C.-H. Wang, L. Jiang, and H. X. Tang, Waveguide cavity optomagnonics for microwave-to-optics conversion, Optica **7**, 1291 (2020).

[31] N. Zhu, X. Zhang, X. Han, C.-L. Zou, and H. X. Tang, Inverse Faraday effect in an optomagnonic waveguide, Phys. Rev. Appl. **18**, 024046 (2022).

[32] J. R. Everts, M. C. Berrington, R. L. Ahlefeldt, and J. J. Longdell, Microwave to optical photon conversion via fully concentrated rare-earth-ion crystals, Phys. Rev. A **99**, 063830 (2019).

[33] M. C. Berrington, M. J. Sellars, J. J. Longdell, H. M. Rønnow, H. H. Vallabhapurapu, C. Adambukulam, A. Laucht, and R. L. Ahlefeldt, Negative refractive index in dielectric crystals containing stoichiometric rare-earth ions, Adv. Opt. Mater. **11**, 2301167 (2023).

[34] T. S. Parvini, V. A. S. V. Bittencourt, and S. V. Kusminskiy, Antiferromagnetic cavity optomagnonics, Phys. Rev. Res. **2**, 022027 (2020).

[35] M. Hiraishi, Z. H. Roberts, G. G. G. King, L. S. Trainor, and J. J. Longdell, Long optical coherence times in a rare-earth-doped antiferromagnet, Nat. Phys. **21**, 1112 (2025).

[36] M. Levy, R. M. Osgood Jr., F. J. Rachford, A. Kumar, and H. Bakhru, Narrow-linewidth yttrium iron garnet films for heterogeneous integration, MRS Online Proc. Library **603**, 119 (1999).

[37] G. Schmidt, C. Hauser, P. Trempler, M. Paleschke, and E. T. Papaioannou, Ultra thin films of yttrium iron garnet with very low damping: A review, Physica Status Solidi B **257**, 1900644 (2020).

[38] L. K. C. S. Assis, J. E. Abrão, A. S. Carvalho, L. A. P. Gonçalves, A. Galembeck, and E. Padrón-Hernández, The FMR line width and the structure in YIG films deposited by MOD on silicon (1 0 0), J. Magn. Magn. Mater. **568**, 170388 (2023).

[39] C. W. Zollitsch, S. Khan, V. T. T. Nam, I. A. Verzhbitskiy, D. Sagkovits, J. O'Sullivan, O. W. Kennedy, M. Strungaru, E. J. G. Santos, J. J. L. Morton, G. Eda, and H. Kurebayashi, Probing spin dynamics of ultra-thin van der Waals magnets via photon-magnon coupling, Nat. Commun. **14**, 2619 (2023).

[40] T. Böttger, C. W. Thiel, Y. Sun, and R. L. Cone, Optical decoherence and spectral diffusion at 1.5 µm in $Er^{3+}:Y_2SiO_5$ versus magnetic field, temperature, and Er^{3+} concentration, Phys. Rev. B **73**, 075101 (2006).

[41] T. Zhong, J. M. Kindem, E. Miyazono, and A. Faraon, Nanophotonic coherent light–matter interfaces based on rare-earth-doped crystals, Nat. Commun. **6**, 8206 (2015).

[42] N. Kukharchyk, D. Sholokhov, O. Morozov, S. L. Korableva, A. A. Kalachev, and P. A. Bushev, Optical coherence of $^{166}Er{:}\,^{7}LiYF_4$ crystal below 1 K, New J. Phys. **20**, 023044 (2018).

[43] C. M. Phenicie, P. Stevenson, S. Welinski, B. C. Rose, A. T. Asfaw, R. J. Cava, S. A. Lyon, N. P. de Leon, and J. D. Thompson, Narrow optical line widths in erbium implanted in TiO_2, Nano Lett. **19**, 8928 (2019).

[44] E. Lafitte-Houssat, A. Ferrier, S. Welinski, L. Morvan, M. Afzelius, P. Berger, and P. Goldner, Optical and spin inhomogeneous linewidths in $^{171}Yb^{3+}:Y_2SiO_5$, Opt. Mater. X **14**, 100153 (2022).

[45] P. Stevenson, C. M. Phenicie, I. Gray, S. P. Horvath, S. Welinski, A. M. Ferrenti, A. Ferrier, P. Goldner, S. Das, R. Ramesh, R. J. Cava, N. P. de Leon, and J. D. Thompson, Erbium-implanted materials for quantum communication applications, Phys. Rev. B **105**, 224106 (2022).

[46] N. Kalb, A. A. Reiserer, P. C. Humphreys, J. J. W. Bakermans, S. J. Kamerling, N. H. Nickerson, S. C. Benjamin, D. J. Twitchen, M. Markham, and R. Hanson, Entanglement distillation between solid-state quantum network nodes, Science **356**, 928 (2017).

[47] A. Kamra, W. Belzig, and A. Brataas, Magnon-squeezing as a niche of quantum magnonics, Appl. Phys. Lett. **117**, 090501 (2020).

[48] I. C. Skogvoll, J. Lidal, J. Danon, and A. Kamra, Tunable anisotropic quantum Rabi model via a magnon–spin-qubit ensemble, Phys. Rev. Appl. **16**, 064008 (2021).

[49] C. Kittel, On the theory of ferromagnetic resonance absorption, Phys. Rev. **73**, 155 (1948).

[50] C. Kittel, *Introduction to Solid State Physics*, 8th ed. (John Wiley & Sons, New York, 2004).

[51] See Supplemental Material at http://link.aps.org/supplemental/10.1103/kqw2-gs9c for a detailed description of the Hamiltonian in different notations, the solution to the equations of motion using the adiabatic elimination approximation and input-output formalism, and a comprehensive list of the parameters and assumptions used in the calculations.

[52] D. F. Walls and G. J. Milburn, *Quantum Optics*, 2nd ed. (Springer, Berlin, 2008).

[53] M. P. Fewell, Adiabatic elimination, the rotating-wave approximation and two-photon transitions, Opt. Commun. **253**, 125 (2005).

[54] E. Brion, L. H. Pedersen, and K. Mølmer, Adiabatic elimination in a lambda system, J. Phys. A: Math. Theor. **40**, 1033 (2007).

[55] B. T. Torosov and N. V. Vitanov, Adiabatic elimination of a nearly resonant quantum state, J. Phys. B: At. Mol. Opt. Phys. **45**, 135502 (2012).

[56] L. A. Williamson, Y.-H. Chen, and J. J. Longdell, Magneto-optic modulator with unit quantum efficiency, Phys. Rev. Lett. **113**, 203601 (2014).

[57] X. Li, M. Bamba, N. Yuan, Q. Zhang, Y. Zhao, M. Xiang, K. Xu, Z. Jin, W. Ren, G. Ma, S. Cao, D. Turchinovich, and J. Kono, Observation of Dicke cooperativity in magnetic interactions, Science **361**, 794 (2018).

[58] Y. Cho, S. Kang, Y. W. Nahm, A. Y. Mohamed, Y. Kim, D.-Y. Cho, and S. Cho, Structural, optical, and magnetic properties of erbium-substituted yttrium iron garnets, ACS Omega **7**, 25078 (2022).

[59] J. Everts, Investigation of fully concentrated rare-earth crytals for microwave upconversion, Masters thesis, University of Otago, 2020.

[60] M. H. Cohen and F. Keffer, Dipolar sums in the primitive cubic lattices, Phys. Rev. **99**, 1128 (1955).

[61] M. H. Cohen and F. Keffer, Erratum: Dipolar sums in the primitive cubic lattices [Phys. Rev. 99, 1128 (1955)], Phys. Rev. B **10**, 787(E) (1974).

[62] M. G. Cottam, Theory of dipole-dipole interactions in ferromagnets. I. The thermodynamic properties, J. Phys. C **4**, 2658 (1971).

[63] T. Böttger, Y. Sun, C. W. Thiel, and R. L. Cone, Spectroscopy and dynamics of $Er^{3+}:Y_2SiO_5$ at 1.5 μm, Phys. Rev. B **74**, 075107 (2006).

[64] Y. Sun, T. Böttger, C. W. Thiel, and R. L. Cone, Magnetic g tensors for the $^4I_{15/2}$ and $^4I_{13/2}$ states of $Er^{3+}:Y_2SiO_5$, Phys. Rev. B **77**, 085124 (2008).

[65] M. Pechal and A. H. Safavi-Naeini, Millimeter-wave interconnects for microwave-frequency quantum machines, Phys. Rev. A **96**, 042305 (2017).